Applied Physics Express

The Japan Society of Applied Physics

OPEN ACCESS

# Metal resist for extreme ultraviolet lithography characterized by scanning transmission electron microscopy

To cite this article: Minoru Toriumi *et al* 2016 *Appl. Phys. Express* **9** 031601

View the article online for updates and enhancements.

You may also like

- *(Invited)* Effect of Junction Resistance on the Percolation Conductivity of Metal Nanowire Networks for Transparent Conductors
Shreshtha Mishra, Ying Xue, Nicholas Fata et al.
- Low Temperature Methane Combustion Catalysts for Pellistors Investigated By Simultaneous Thermal Analysis
Olena Yurchenko, Hans-Fridtjof Pernau, Benedikt Bierer et al.
- High Performance Photoresist Planarization Process by CMP with Resin Abrasive for Trench-First Cu/Low-*k* Dual Damascene Process
Yukiteru Matsui, Satoko Seta, Masako Kinoshita et al.

This content was downloaded from IP address 3.145.173.112 on 23/04/2024 at 08:21

OPEN ACCESS

Applied Physics Express 9, 031601 (2016)

http://doi.org/10.7567/APEX.9.031601

# Metal resist for extreme ultraviolet lithography characterized by scanning transmission electron microscopy

Minoru Toriumi[1]*, Yuta Sato[2]*, Masanori Koshino[2], Kazu Suenaga[2], and Toshiro Itani[1]

[1]*Advanced Resist Research Department, EUVL Infrastructure Development Center, Inc. (EIDEC), Tsukuba, Ibaraki 305-8569, Japan*

[2]*Nanomaterials Research Institute, National Institute of Advanced Industrial Science and Technology (AIST), Tsukuba, Ibaraki 305-8565, Japan*

*E-mail: minoru.toriumi@eidec.co.jp; yuta-sato@aist.go.jp

Received December 22, 2015; accepted January 13, 2016; published online January 29, 2016

We characterized the structures of metal resists used in EUV lithography by low-voltage aberration-corrected scanning transmission electron microscopy (STEM) combined with electron energy-loss spectroscopy (EELS). This study presents the first atomic-level observation of resist components in resist film. The structures of metal (zirconium or titanium) oxide cores are unambiguously identified, and the local elemental distribution in the resist film is obtained. The initial size of zirconium oxide cores is well maintained in the resist film. However, titanium oxide cores tend to aggregate to form an indefinite structure. The spatial distribution of metal cores may influence lithographic characteristics.
© 2016 The Japan Society of Applied Physics

The trend in optical lithography is that smaller is better. A demand for smaller patterning in semiconductor devices has led to the use of shorter-wavelength light sources in lithography for the fabrication of high-density and high-performance semiconductor devices. EUV lithography[1,2] has received attention as the next-generation method that uses wavelengths as small as 13.5 nm. However, the low power of EUV light sources limits EUV exposure tool technology[3–5] and necessitates the use of highly sensitive EUV resist materials. Therefore, the development of EUV resist materials continues to be a critical challenge for the implementation of EUV lithography.[6–8]

Some important properties of resist materials that must meet certain requirements include resolution, line-edge roughness, and sensitivity.[9] Conventional, chemically amplified resists have been studied for use as EUV resists.[10,11] New metal resists[12–19] were reported to offer superior resolution,[12,13] sensitivity,[14–16] and etching resistance,[12] and have good shelf-life stability,[19] but none meets all the requirements simultaneously. Our group at EIDEC has developed a metal resist that comprises a metal oxide core and an organic molecule shell.[7] Figure 1 shows typical scanning electron microscopy (SEM) images of the line patterns of the EIDEC metal resist. This metal resist has good sensitivity of 9 mJ/cm$^2$, which is a very important property for obtaining high throughput with the low-intensity EUV light sources currently available. The finest line pattern in Fig. 1(a) has a line width of 11 nm and a line pitch of 120 nm, but the resolution and line-edge roughness need to be further improved.

Transmission electron microscopy (TEM) as well as semiconductor device inspections[20] have been used to characterize resist materials for EUV lithography. Cross-sectional TEM images of metal resist line patterns provide information on device structure and material morphology.[21] It is also important to understand the spatial distribution of the shells of organic molecules that surround individual metal oxide cores in the resists, which conventional TEM techniques have been unable to show. Recently, the use of aberration-corrected scanning TEM (STEM) at low electron-accelerating voltages has provided atomistic information such as atomic positions and electronic states in nanomaterials without seriously damaging their structures as occurs with electron beam irradiation.[22] The structures and reaction mechanisms of metal resists can be characterized in further detail using the latest techniques, enabling the development of new resist materials with improved resist properties. In this study, we demonstrate atomic-level imaging and elemental identification of metal resists using low-voltage aberration-corrected STEM.

The metal resist materials evaluated in this study were composed of metal oxide nanoparticles and organic molecules forming a core–shell state. Zirconium oxide ($ZrO_x$) and titanium oxide ($TiO_x$) were selected as the metal oxide cores and methacrylic acid (MAA) was used as a component of the shell. The metal resist materials were synthesized using the sol–gel method. The resist solutions were prepared by adding appropriate amounts of the nanoparticle powder to propylene glycol monomethyl ether acetate (PGMEA).

Light scattering measurements with a Zetasizer Nano ZS (Malvern Instruments) evaluated the size of the metal resist particles in the PGMEA solution. The refractive index and viscosity of PGMEA at 20 °C were 1.402 and 1.200 mPa·s, respectively. The refractive index of $ZrO_2$ was 2.17 and the refractive index and absorption coefficient of $TiO_2$ were 1.95 and 0.01, respectively. The metal element content in the metal resists was analyzed by inductively coupled plasma atomic emission spectroscopy using a Seiko Instruments SPS400. The carbon and hydrogen contents of the resist powder were determined simultaneously using a vario MICRO cube system (Elementar Analysensysteme).

STEM images of the metal resists were obtained using a JEOL JEM-2100F transmission electron microscope, equipped with DELTA spherical aberration correctors,[23] at an electron-accelerating voltage of 60 kV. Energy dispersive X-ray spectrometry (EDS) and electron energy-loss spectroscopy (EELS) analyses were performed using JEOL Centurio silicon drift detectors and a Gatan quantum spectrometer, respectively, installed on the microscope. For STEM analyses, each metal resist solution was dropped onto a molybdenum microgrid coated with an amorphous carbon film with holes and air-dried at 20 °C. The microgrid was

Content from this work may be used under the terms of the Creative Commons Attribution 4.0 license. Any further distribution of this work must maintain attribution to the author(s) and the title of the work, journal citation and DOI.


© 2016 The Japan Society of Applied Physics

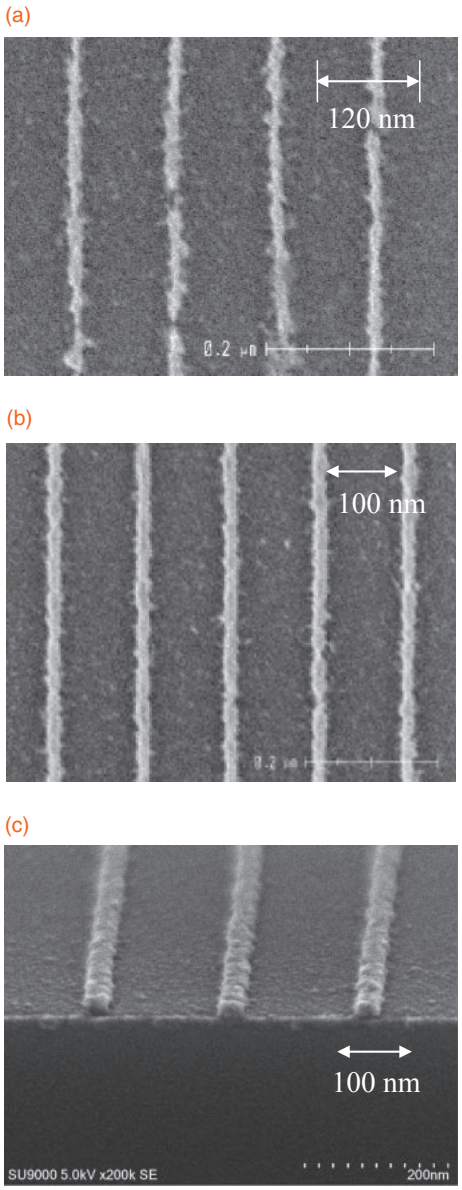


**Fig. 1.** (a) SEM photo exposed using HSFET (NA = 0.5, quadrupole illumination) of the isolated line pattern of a EIDEC metal resist with a width of 11 nm and a pitch of 120 nm exposed at 9 mJ/cm$^2$. (b) SEM photo of 1:5 dense line and space patterns of EIDEC metal resist with a 22 nm line width exposed at 14 mJ/cm$^2$. (c) Cross-sectional SEM photo of 1:5 line and space patterns of EIDEC metal resist with a 32 nm line width exposed at 13 mJ/cm$^2$.

then heated at 80 °C for 1 h in a vacuum to eliminate volatile species, such as residual PGMEA solvent, prior to STEM observation. Commercially available nanoparticles of $ZrO_2$ (Wako Pure Chemical Industries) and $TiO_2$ (Ishihara Sangyo) were used as references for EELS analysis.

First, we examined the line patterning of the $ZrO_x$–MAA resist. Spin-coated films of the resist on silicon wafers were delineated using a High-NA small field exposure tool (HSFET; NA = 0.5, quadrupole illumination) at EIDEC and developed for 30 s with *n*-butyl acetate. Satisfactory patterning properties (Fig. 1) were achieved with the $ZrO_x$–MAA resist. The post-coating delay of the $ZrO_x$ resist was comparatively better than that of the $TiO_x$–MAA resist.

We then characterized these two metal resists using STEM to further understand the differences between their line-patterning properties with respect to their morphology.

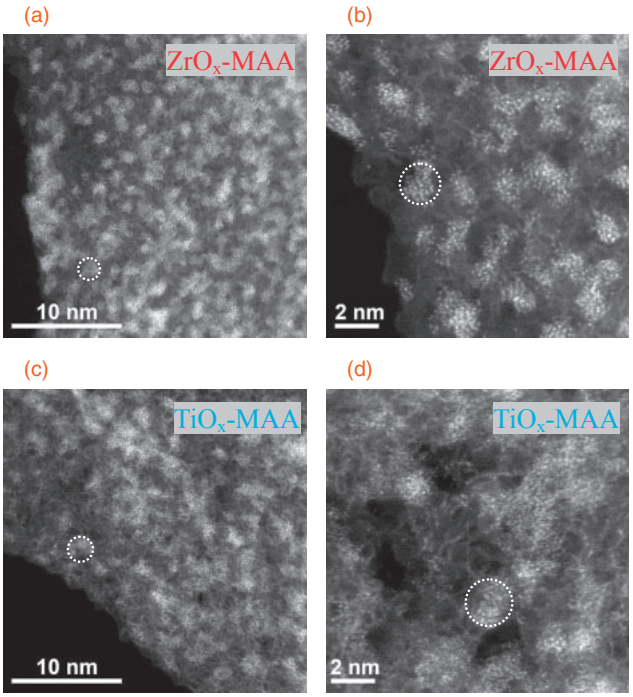


**Fig. 2.** (a) Low- and (b) high-magnification ADF-STEM images of $ZrO_x$–MAA resist and (c) low- and (d) high-magnification ADF-STEM images of $TiO_x$–MAA resist supported on amorphous carbon. Dotted circles show the diameters of (a, b) 2.0 nm and (c, d) 2.3 nm determined by optical scattering methods.

Figure 2 shows annular dark field (ADF) STEM images of $ZrO_x$–MAA and $TiO_x$–MAA resist layers on amorphous carbon substrate films. The brightness of the detected zirconium and titanium atoms is greater, depending on their atomic numbers ($Z = 40$ and 22, respectively), than that of carbon and oxygen atoms, enabling us to understand the morphology of the metal oxide cores. Figures 2(a) and 2(b) show that individual $ZrO_x$ cores are separated from each other, and their apparent sizes are in good agreement with the average diameter of 2.0 nm measured by light scattering in the solution phase. In contrast, Figs. 2(c) and 2(d) show that $TiO_x$ cores are not clearly separated from each other. Although the average diameter of $TiO_x$ cores is 2.3 nm based on light scattering in the solution phase, the $TiO_x$ cores tend to aggregate into larger clusters with indefinite shapes as the PGMEA solvent is eliminated. The high-magnification images in Figs. 2(b) and 2(d) clearly show that the structures of both $ZrO_x$ and $TiO_x$ cores are amorphous. While electron beam irradiation of metal resists under conventional TEM conditions can cause the crystallization of metal oxide cores,[21] the STEM observation at a reduced electron-accelerating voltage of 60 kV preserved the amorphous nature of $ZrO_x$ and $TiO_x$ cores, even after high-magnification imaging.

The difference in the distributions of the $ZrO_x$ and $TiO_x$ cores is attributed to their affinity to the surrounding MAA molecules, the PGMEA solvent, or both, and to the interactions between the cores. Since inhomogeneity of the components in the resist film is crucial in determining such properties as resolution, line-edge roughness, and sensitivity,[24] techniques to evaluate the homogeneity of metal resists are important for the development of improved resist materials. The images presented in Fig. 2 prove that low-voltage STEM


© 2016 The Japan Society of Applied Physics

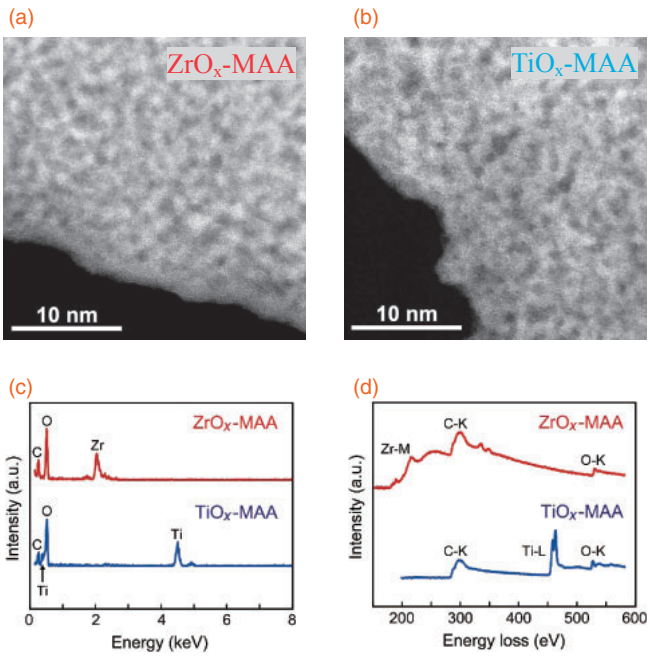


**Fig. 3.** ADF-STEM images of a freestanding film of (a) $ZrO_x$–MAA and (b) $TiO_x$–MAA resists. (c) EDS and (d) EELS spectra of a freestanding film of $ZrO_x$–MAA and $TiO_x$–MAA resists.

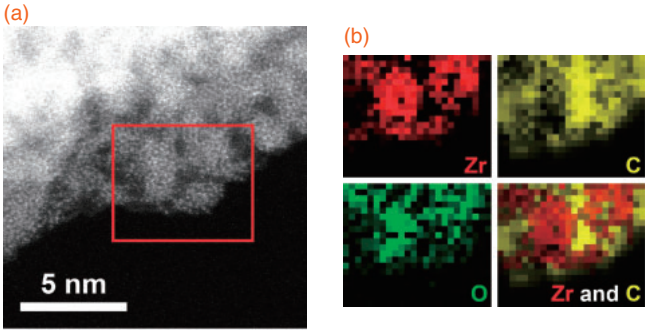


**Fig. 4.** (a) ADF-STEM image of a freestanding film of $ZrO_x$–MAA resist. (b) Elemental maps of zirconium (Zr), carbon (C), oxygen (O), and superposition of Zr and C obtained by EELS in the boxed area in (a).

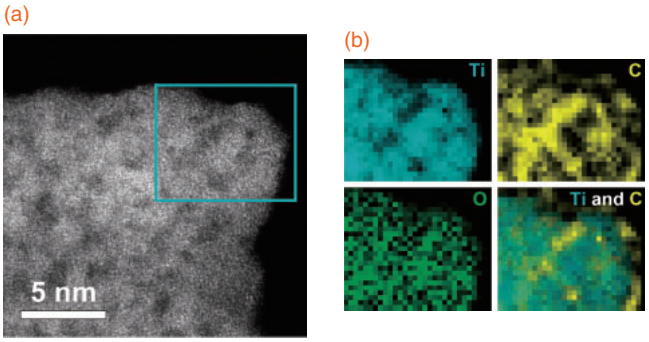


**Fig. 5.** (a) ADF-STEM image of a freestanding film of $TiO_x$–MAA resist. (b) Elemental maps of titanium (Ti), carbon (C), oxygen (O), and superposition of Ti and C obtained by EELS in the boxed area in (a).

enables unambiguous visualization of individual metal oxide cores and their local distribution without seriously damaging their structures.

The chemical composition of the metal resists was examined by EDS and EELS. To exclude signals from the amorphous carbon substrate films on the microgrids, freestanding areas of the resist layers covering the microgrid holes were carefully chosen for the measurements. Figures 3(a) and 3(b) are ADF-STEM images showing the edges of such freestanding areas of $ZrO_x$–MAA and $TiO_x$–MAA resist layers, respectively. Because the resist layers in these selected areas are thicker than those shown in Fig. 2, even $ZrO_x$ cores are not clearly identified as isolated particles in Fig. 3(a).

Figure 3(c) shows typical EDS spectra of the $ZrO_x$–MAA and $TiO_x$–MAA resist layers. The spectral peaks are ascribed to the emission lines of carbon K$\alpha$ (0.28 keV), oxygen K$\alpha$ (0.53 keV), zirconium L (2.04 keV), and titanium L, K$\alpha$, and K$\beta$ (0.45, 4.51, and 4.93 keV, respectively) in accordance with the components of the resists. The average Zr/C and Zr/O atomic ratios of the $ZrO_x$–MAA resist were estimated on the basis of EDS analysis to be 0.50 and 0.38, respectively. The average Ti/C and Ti/O atomic ratios of the $TiO_x$–MAA resist were estimated to be 0.73 and 0.32, respectively. Oxygen atoms of the metal oxide cores and the MAA shells cannot be distinguished to estimate these atomic ratios.

Figure 3(d) shows typical EELS spectra of the $ZrO_x$–MAA and $TiO_x$–MAA resist layers. In addition to the carbon and oxygen K edges at approximately 284 and 532 eV, respectively, the zirconium M edge starts to appear at approximately 180 eV in the spectrum of the $ZrO_x$–MAA resist, and the titanium L edge is observed at approximately 456 eV for the $TiO_x$–MAA resist. The observed profiles of the zirconium M and titanium L edges are in good agreement with those found for the control samples of $ZrO_2$ and $TiO_2$ nanoparticles, respectively, confirming that these metals exist as oxides in the resist layers (see Fig. S1 in the online supplementary data at http://stacks.iop.org/APEX/9/031601/mmedia). The average Zr/C and Zr/O atomic ratios of the $ZrO_x$–MAA resist were estimated on the basis of EELS analysis to be 0.65 and 0.41, respectively. The average Ti/C and Ti/O atomic ratios of the $TiO_x$–MAA resist were estimated to be 0.88 and 0.42, respectively.

EDS and EELS analyses proved that the Ti/C atomic ratio in the $TiO_x$–MAA resist layer was 1.4–1.5 times greater than the Zr/C ratio in the $ZrO_x$–MAA layer. Assuming that all carbon atoms detected in the resist layers existed as MAA molecules, MAA/$ZrO_x$ and MAA/$TiO_x$ molar ratios were estimated to be 0.38–0.50 and 0.29–0.34, respectively. These molar ratios were equal to 1.5 in the original resist solutions, but two-thirds or more of the MAA molecules were eliminated together with the PGMEA during preparation of the dried resist layers prior to STEM analyses. The $ZrO_x$–MAA resist layer was found to contain more MAA than the $TiO_x$–MAA resist layer, suggesting that $ZrO_x$ cores exhibit a higher affinity to MAA.

Elemental distribution in the metal resist layers was further analyzed by STEM–EELS chemical mapping. Figures 4(a) and 5(a) show the ADF-STEM images of freestanding $ZrO_x$–MAA and $TiO_x$–MAA resist layers, respectively, that were selected for analysis. EELS images were acquired from the boxed areas indicated in the figures, and elemental distributions were determined on the basis of the intensities of carbon and oxygen K edges and zirconium M or titanium L edge


© 2016 The Japan Society of Applied Physics

at each measured point. Figure 4(b) shows the elemental maps for the selected area of the $ZrO_x$–MAA resist layer in Fig. 4(a). Individual $ZrO_x$ cores that appear as bright regions in the ADF-STEM image are also clearly seen in the zirconium map. The carbon map profile is distinctly different from that of the zirconium map. The signal intensity of carbon is higher in the space between the $ZrO_x$ cores, suggesting that MAA-based components are concentrated there. Oxygen atoms exist in both the $ZrO_x$ cores and MAA molecules but are more concentrated around the cores as determined from the observed higher signal intensity in the oxygen map.

Figure 5(b) shows the elemental maps for the selected area of the $TiO_x$–MAA resist layer in Fig. 5(a). Individual $TiO_x$ cores are not separately identified in the titanium map because of aggregation that is suggested by the contrast profile in the ADF-STEM image. Examination of the carbon map clearly shows that MAA-based components exist mainly in the gap between the aggregated $TiO_x$ cores. Oxygen is detected in both the $TiO_x$ cores and the MAA region; its distribution is relatively uniform even though its signal intensity is lower than that of the other elements.

The STEM–EELS chemical mapping proves that both $ZrO_x$–MAA and $TiO_x$–MAA resist layers are actually composites of metal oxide cores and MAA molecules with the spaces between the metal oxide cores occupied by MAA. $ZrO_x$ cores were found as individual nanoparticles, while aggregation of $TiO_x$ cores was confirmed by the titanium map of the $TiO_x$–MAA resist layer. In metal oxide-based resists, carboxyl groups of the surrounding organic molecules such as MAA are expected to be bound to a metal oxide core, resulting in a core–shell state.[14] The present study suggests that such a core–shell state is maintained in a more stable condition for the $ZrO_x$–MAA resist than for the $TiO_x$–MAA resist, even during the process of PGMEA solvent elimination, preventing $ZrO_x$ core aggregation. The excellent post-coating delay of $ZrO_x$–MAA compared to that of $TiO_x$–MAA is reasonably well explained by these models.

In conclusion, we have demonstrated atomic-level imaging and elemental identification of metal resists using low-voltage aberration-corrected STEM. To the best of our knowledge, this study is the first atomic-level observation of resist components in resist films. STEM observed the morphology of the metal resist film, and the resist component of a single core of $ZrO_x$ was identified as an isolated nanoparticle, while $TiO_x$ cores were found to be aggregated. The morphologies of each component in the resist films may influence lithographic properties such as resolution, line-edge roughness, and sensitivity, in addition to the post-coating delay. The inhomogeneity of resist components, such as photoacid generators and quenchers, is being examined as it becomes more important for the delineation of single nanometer patterns.[24] STEM is a useful tool for the visualization and atomistic study of resist materials. Further study of the role of shell molecules in metal resists is underway.

**Acknowledgments** MT and TI acknowledge EIDEC member companies for their continued support. This study was supported by the New Energy and Industrial Technology Development Organization (NEDO) and the Ministry of Economy, Trade and Industry (METI). YS, MK, and KS acknowledge support from the JST Research Acceleration Program.

1) S. Wurm, Jpn. J. Appl. Phys. **46**, 6105 (2007).
2) W. Montgomery, J. S. Chun, M. Liehr, and M. Tittnich, Proc. SPIE **9422**, 94221L (2015).
3) V. Y. Banine, K. N. Koshelev, and G. H. P. M. Swinkels, J. Phys. D **44**, 253001 (2011).
4) A. A. Schafgans, D. J. Brown, I. V. Fomenkov, R. Sandstrom, A. Ershov, G. Vaschenko, R. Rafac, M. Purvis, S. Rokitski, Y. Tao, D. J. Riggs, W. J. Dunstan, M. Graham, N. R. Farrar, D. C. Brandt, N. Böwering, A. Pirati, N. Harned, C. Wagner, H. Meiling, and R. Kool, Proc. SPIE **9422**, 94220B (2015).
5) H. Mizoguchi, H. Nakarai, T. Abe, K. Nowak, Y. Kawasuji, H. Tanaka, Y. Watanabe, T. Hori, T. Kodama, Y. Shiraishi, T. Yanagida, G. Soumagne, T. Yamada, T. Yamazaki, S. Okazaki, and T. Saitou, Proc. SPIE **9422**, 94220C (2015).
6) D. De Simone, A.-M. Goethals, F. V. Roey, T. Zheng, P. Foubert, E. Hendrickx, G. Vandenberghe, and K. Ronse, J. Photopolym. Sci. Technol. **27**, 601 (2014).
7) T. Itani and T. Kozawa, Jpn. J. Appl. Phys. **52**, 010002 (2013).
8) ITRS, International Technology Roadmap for Semiconductors [http://www.itrs.net/].
9) C. D. Higgins, C. R. Szmanda, A. Antohe, G. Denbeaux, J. Georger, and R. L. Brainard, J. Appl. Phys. **50**, 036504 (2011).
10) H. Ito, Adv. Polym. Sci. **172**, 37 (2005).
11) H. Nakagawa, T. Naruoka, and T. Nagai, J. Photopolym. Sci. Technol. **27**, 739 (2014).
12) D. De Simone, I. Pollentier, and G. Vandenberghe, J. Photopolym. Sci. Technol. **28**, 507 (2015).
13) A. Grenville, J. T. Anderson, B. L. Clark, P. De Schepper, J. Edson, M. Greer, K. Jiang, M. Kocsis, S. T. Meyers, J. K. Stowers, A. J. Telecky, D. De Simone, and G. Vandenberghe, Proc. SPIE **9425**, 94250S (2015).
14) J. Jiang, B. Zhang, M. Yu, L. Li, M. Neisser, J. S. Chun, E. P. Giannelis, and C. K. Ober, J. Photopolym. Sci. Technol. **28**, 515 (2015), and references therein.
15) E. Buitrago, O. Yildirim, C. Verspaget, N. Tsugama, R. Hoefnagels, G. Rispens, and Y. Ekinci, Proc. SPIE **9422**, 94221S (2015).
16) J. Passarelli, M. Murphy, R. Del Re, M. Sortland, L. Dousharm, M. Vockenhuber, Y. Ekinci, M. Neisser, D. Freedman, and R. Brainard, Proc. SPIE **9425**, 94250T (2015).
17) M. Sortland, R. Del Re, J. Passarelli, J. Hotalen, M. Vockenhuber, Y. Ekinci, M. Neisser, D. Freedman, and R. Brainard, Proc. SPIE **9422**, 942227 (2015).
18) M. Neisser, K. Cummings, S. Valente, C. Montgomery, Y.-J. Fan, K. Matthews, J. S. Chun, and P. D. Ashby, Proc. SPIE **9422**, 94220L (2015).
19) M. Krysak, M. Leeson, E. Han, J. Blackwell, and S. Harlson, Proc. SPIE **9422**, 942205 (2015).
20) K. Takamasu, H. Okitou, S. Takahashi, O. Inoue, H. Kawada, V. Kamineni, A. Paul, and A. F. Bello, Proc. SPIE **9050**, 90501K (2014).
21) R. P. Oleksak, R. E. Ruther, F. Luo, K. C. Fairley, S. R. Decker, W. F. Stickle, D. W. Johnson, E. L. Garfunkel, G. S. Herman, and D. A. Keszler, ACS Appl. Mater. Interfaces **6**, 2917 (2014).
22) K. Suenaga and M. Koshino, Nature **468**, 1088 (2010).
23) T. Sasaki, H. Sawada, F. Hosokawa, Y. Kohno, T. Tomita, T. Kaneyama, Y. Kondo, K. Kimoto, Y. Sato, and K. Suenaga, J. Electron Microsc. (Tokyo) **59**, 1 (2010).
24) M. Toriumi and T. Itani, Jpn. J. Appl. Phys. **54**, 06FE02 (2015).


© 2016 The Japan Society of Applied Physics